Filament Eruption from Active Region 13283 Leading to a Fast Halo-CME and an Intense Geomagnetic Storm on 2023 April 23

P. Vemareddy ⬤
Indian Institute of Astrophysics, II Block, Koramangala, Bengaluru-560 034, India
Received 2023 September 13; revised 2023 December 9; accepted 2023 December 14; published 2024 January 26

Abstract

Using multi-instrument and multiwavelength observations, we studied a coronal mass ejection (CME) that led to an intense geomagnetic storm on 2023 April 23. The eruption occurred on April 21 in solar active region (AR) 13283 near the disk center. The AR was in its decay stage, with fragmented polarities and a preexisting long filament channel a few days before the eruption. The study of the magnetic field evolution suggests that the flux rope (filament) was built up by monotonous helicity accumulation over several days, and furthermore, converging and canceling fluxes led to a change in helicity injection, resulting in an unstable nature of the magnetic flux rope (MFR) and its further eruption. Importantly, the CME morphology revealed that the MFR apex underwent a rotation of up to $56°$ in clockwise direction owing to its positive helicity. The CME decelerates in the field of view (FOV) of the Large Angle Spectrometric Coronagraph and has a plane-of-sky velocity of $1226 \, \mathrm{km \, s^{-1}}$ at $20 \, R_\odot$. In the FOV of the Heliospheric Imager, the lateral expansion of the CME is tracked better than the earthward motion. This implies that the arrival time is difficult to assess. The in situ arrival of the interplanetary CME shock was at 07:30 UT on April 23, and a geomagnetic storm commenced at 08:30 UT. The flux rope fitting to the in situ magnetic field observations reveals that the magnetic cloud flux rope orientation is consistent with its near-Sun orientation, which has a strong negative Bz-component. The analysis of this study indicates that the near-Sun rotation of the filament during its eruption to the CME is the key to the negative Bz-component and consequently the intense geomagnetic storm.

Unified Astronomy Thesaurus concepts: The Sun (1693)

Supporting material: animations

1. Introduction

Coronal mass ejections (CMEs) are large-scale magnetized plasma structures originating from the Sun. They propagate outward through interplanetary space, affecting the planetary atmospheres (e.g., Webb & Howard 2012). Their propagation toward Earth was established to be the cause of the most severe geomagnetic disturbances on Earth (e.g., Gosling et al. 1991; Gosling 1993; Webb et al. 2000; Zhang et al. 2007). Therefore, it is of scientific and technological interest to understand the complete picture of CMEs, including their magnetic structure and the mechanisms involved in their origin from the source regions, their evolution, and their propagation from the Sun to the Earth (Zhang et al. 2021).

Historically, CMEs have been observed in the images of white-light coronagraphs on board OSO7 (MacQueen et al. 1974), Skylab (Sheeley et al. 1980), and the Solar Maximum Mission (House et al. 1981). When a CME occurs, coronagraphs use Thomson-scattered light from free electrons in the coronal and heliospheric plasma to observe the outward flow of density structures coming from the Sun. Following these early space coronagraphs, the Large Angle Spectrometric Coronagraph (LASCO) on board board SoHO, launched in 1995, is still continuously capturing white-light observations of the Sun. From 2006, the coronagraph instruments on board the twin Solar-Terrestrial and Relational Observatory (STEREO; Howard et al. 2008) spacecraft started providing vantage point

white-light images in a much wider field of view (FOV), enabling us to track the CME propagation up to $330 \, R_\odot$. The CMEs in white-light images are often observed in association with filament or prominence structures (e.g., Webb & Hundhausen 1987; Gopalswamy et al. 2003; Vemareddy et al. 2012b, 2017), X-ray sigmoids (Canfield et al. 1999; Moore et al. 2001; Vasantharaju et al. 2019), and extreme-ultraviolet (EUV) hot channels (e.g., Zhang et al. 2012; Cheng et al. 2013; Vemareddy & Zhang 2014; Vemareddy et al. 2022) from the solar disk. Therefore, white-light observations of the CMEs are frequently accompanied by eruptions from the solar disk, e.g., by the GONG Hα telescope, the SOHO Extreme Ultraviolet Imaging Telescope, the STEREO Extreme-Ultra-Violet Imager (EUVI), and the recently launched Solar Dynamics Observatory (SDO)/AIA instrument. The in situ counterparts of the CMEs are called interplanetary coronal mass ejections (ICMEs), whose observations at 1 au and behind are supplied by the onboard spacecraft instruments, e.g., Voyagers, Ulysses, Helios, Wind, ACE, and STEREO.

The CMEs have a traditional three-part structure, which is usually understood to be compressed plasma in front of a flux rope, a cavity, and a bright filament or prominence surrounding the cavity (Illing & Hundhausen 1985). Therefore, the magnetic configuration of the CME is a magnetic flux rope (MFR) with a helical field that is wound around the central axis. After ejection, the CME largely maintains its magnetic configuration or topology as a twisted MFR, and it is therefore able to continuously propagate outward through the heliosphere, interacting with the ambient solar wind. The statistical study by Vourlidas et al. (2013) suggests that at least 40% of CMEs observed by space-borne instruments have a clear MFR

structure. According to many studies based on satellite and ground-based data, this MFR structure in the outer corona is thought to be an evolved form of the magnetic structure of filaments observed in Hα or sigmoidal structures in soft X-rays in the source regions.

Geoeffective CMEs are those that are directed toward the Earth, and they are called halo CMEs. Therefore, the source region should be near the visible disk center (Srivastava & Venkatakrishnan 2004; Zhang et al. 2007). These front-side halo CMEs associated with strong soft X-ray flares tend to be the most geoeffective (Gopalswamy et al. 2007). After ejection from the inner corona, the CMEs evolve with distinct kinematic, geometric, and magentic properties that determine their geoeffectiveness. The kinematic studies reveal that the CMEs evolve with slow, fast, and gradual acceleration in the inner corona up to 0.1 au (Zhang et al. 2004). The further propagation of the CME in the outer heliosphere is governed solely by the interaction of the CME and the ambient solar wind via aerodynamic drag (Cargill 2004; Vršnak et al. 2010), which causes the faster CMEs to decelerate and slower CMEs to accelerate, tending to equalize their speeds with the speed of the ambient solar wind. Most importantly, the CME is geoeffective when its interplanetary magnetic field points southward, which depends on the orientation of the MFR with respect to the ecliptic. Some CMEs are observed to rotate in the corona due to a variety of mechanisms. Simulations showed the rotation is due to kink instability, and the direction of the rotation depends on the handedness of the magnetic field of the flux rope (Török & Kliem 2003; Lynch et al. 2009). CMEs have also been observed to be deflected both in latitude and longitude (Isavnin et al. 2013). Depending on the relative positions of the coronal features, the deflecting motion was frequently described as being toward the heliospheric current sheet (Cremades & Bothmer 2004) or away from coronal holes (Gopalswamy et al. 2009). These geometric changes of the CMEs in the corona are the key for explaining the CME impact on Earth. For example, Kay et al. (2017) studied the trajectory of the series of CMEs launched from active region (AR) 11158, located near the disk center, and found that only one CME encountered Earth. The other missing CMEs were found to be deflected north up to 30° near the Sun.

In the interest of space-weather impact, identifying the geomagnetic source regions is very important for understanding the characteristics of the magnetic structure that cause the CME eruption and its evolution in the Sun–Earth line. In the 24th solar cycle, only three strong storms occurred with a Dst index < −175 nT, i.e., on 2018 March 17, 2015 June 23, and 2018 August 26 (Gopalswamy et al. 2022). In this study, we study the CME source region of the intense storm that occurred on 2023 April 23 with a Dst Index −212 nT. The source region is identified as AR 13283. An overview of the observations is given in Section 2. The results of the analysis of the magnetic field evolution in the AR, the CME onset mechanism, the CME propagation, and the in situ observations are described in Section 3. A summary of the results with a discussion is provided in Section 4.

2. Overview of Observations

We study the event of a large-scale CME that was launched from AR 13283 on 2023 April 21. We use multispacecraft and multiwavelength observations to study the magnetic

characteristics of the source region, the initiation of the CME from the source region, and its propagation toward Earth.

The source region observations are well covered by the instruments on board the SDO. The Atmospheric Imaging Assembly (Lemen et al. 2012) observes the full disk of the Sun continuously in seven EUV channels. These channels correspond to the chromosphere in the temperature range of around 20,000 K to the corona at 10 million K. The cadence of the observations is 12 s at a pixel scale of $0''.6$. The corresponding magnetic field measurements at the photosphere are obtained from the Helioseismic and Magnetic Imager with a pixel size of $0''.5$. Figure 1(a) displays the full-disk image of the Sun in the AIA 304 Å wave band. The onset of the eruption (CME launch) occurred at around 18:00 UT from AR 13283 and was located near the disk center (S21° W11°), with a long filament channel present along its polarity inversion line (PIL; dashed yellow curve). The observations of the AR in the AIA 131 Å wave band and the corresponding magnetic field measurements at the photosphere are shown in Figures 1(b)–(c). The AR consists of fragmented polarities without one main sunspot, which suggests that the AR is in the decaying phase of its evolution. The solar feature of the explosion manifests itself in the shearing and converging motion of the fluxes along the PIL. In fact, a long filament channel existed before along the PIL of the opposite magnetic fluxes. The eruption feature is a filament as part of this multiply threaded channel. However, the left part of the long filament channel appeared to be unaffected during the eruption.

The white-light observations of the CME are obtained from LASCO (Brueckner et al. 1995) on board the Solar and Heliospheric Observatory (SOHO) as well as from the Sun–Earth Connection Coronal and Heliospheric Investigation (SECCHI; Howard et al. 2008) on board STEREO (Kaiser et al. 2008). LASCO provides white-light images in the FOV of 1.5–6 $R_\odot$ (C2), and 3–32 $R_\odot$ (C3) to study the CME dynamics in the near-Sun corona. The Heliospheric Imager on board SECCHI images the Sun in a much wider FOV (HI1: 15–90 $R_\odot$ and HI2: 70–330 $R_\odot$), and the images are suited to understanding the CME propagation beyond the Earth. At the time of this CME launch, STEREO-A (STA) had a separation angle of 10° with respect to the Earth, so that the CME is viewed with a slightly similar morphology as with LASCO. Figure 1(d) presents the running-difference LASCO/C3 image showing the large-scale halo CME from the AR. The linear speed of the CME projected on the plane of sky is 1284 km s^{-1}, which classifies the CME as a fast CME. CMEs with speeds greater than 960 km s^{-1} and widths greater than 66° are connected with type II radio bursts and are highly geoeffective (Gopalswamy et al. 2001).

The CME is associated with a GOES class M1.7 flare, as indicated by the disk-integrated soft X-ray flux plotted in Figure 2(c). The start, peak, and end times are 17:44 UT, 18:12 UT, and 18:44 UT, respectively. The radio dynamic spectrum obtained from the Radio and Plasma Wave Experiment (WAVES; Bougeret et al. 1995) on board the Wind spacecraft detects the launch of type III radio bursts co-temporal with the flare start and peak times (Figure 2(b)). In addition to type III, the STA/WAVES dynamic spectrum detects type II radio bursts, which arise from shocks driven by CMEs (Cane et al. 1987; Gopalswamy et al. 2019). The shock front is seen to persist up to 20:30 UT, as shown in LASCO white-light images, and correspondingly, the type II emissions are prolonged.
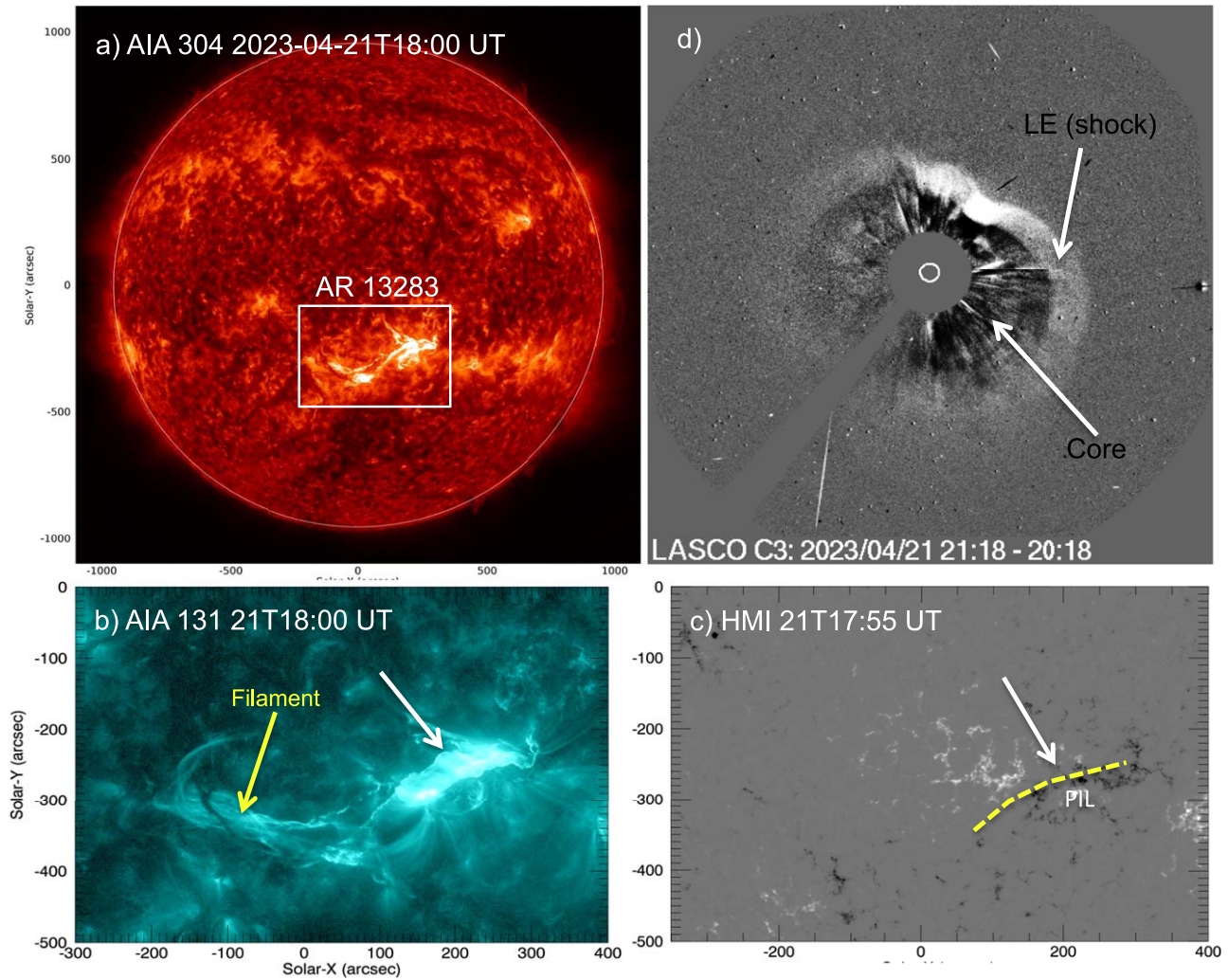
Figure 1. The CME eruption from the Sun that occurred on 2023 April 21, at 18:00 UT. (a) AIA 304 Å image of the Sun showing the location of the AR 13283 (inset) as the source region of the CME eruption. (b) AIA 131 Å images of the AR during the eruption. (c) HMI magnetic field observations of AR 13283. The dashed yellow curve traces the PIL between fragmented opposite magnetic polarities. The long filament channel remains intact, and the erupting feature is a manifestation of the sheared magnetic loops in the vicinity of the PIL. (d) LASCO/C3 running-difference image delineating the Earth-directed halo CME with a bright leading edge and core.

The WIND satellite also records magnetic and plasma observations at the L1 point, which are obtained at a cadence of 92 s. The data demonstrate a distinct in situ counterpart of the CME (ICME) on April 23, with a total field intensity above 30 nT with a rotating magnetic field component. Figure 3(a) depicts the observations of the z-component of the magnetic field (B_z) with respect to time. The shock appears to have hit at 07:30 UT on April 23, with the B_z-component becoming increasingly negative (southward B_z-component). With these observations of the southward B_z, the disturbance storm-time (Dst) index values,[1] as shown in Figure 3(b), indicate the start of a geomagnetic storm. The Dst profile is well correlated with the B_z-component associated with the shock sheath and magnetic cloud regions. The storm peaked at -212 nT around 05:30 UT on April 24. This storm has a Kp index values of up to 8 and is classified as G4 severe. It is the first major storm in solar cycle 25 to cause stunning northern lights (auroras) that extended to lower latitudes around the world.

3. Results

3.1. Magnetic Evolution of the AR

To study the magnetic field evolution in the AR, we obtain a time series (every 12 minutes) of line-of-sight magnetic field observations from the HMI. The magnetic field measurements at each instant in time are projected onto the disk center by the cylindrical equal-area projection method to minimize the projection effects. Then we choose the area of the AR extent such that the footpoints of the loops connected to the filament channel are covered in the evolution time we studied. From these magnetograms, we derive the horizontal velocity of flux motions by using the differential affine velocity estimator (Schuck 2005) method. The velocity field is displayed in Figure 4(a), where horizontal velocities (arrows) are plotted on the Bz images. The contours of 150 G are also overlaid to identify the boundaries of individual polarity regions. The velocity field is spread up to a maximum value of 0.8 km s^{-1}, indicating that different features move at different velocities. We found that emerging flux regions moved apart after their emergence.
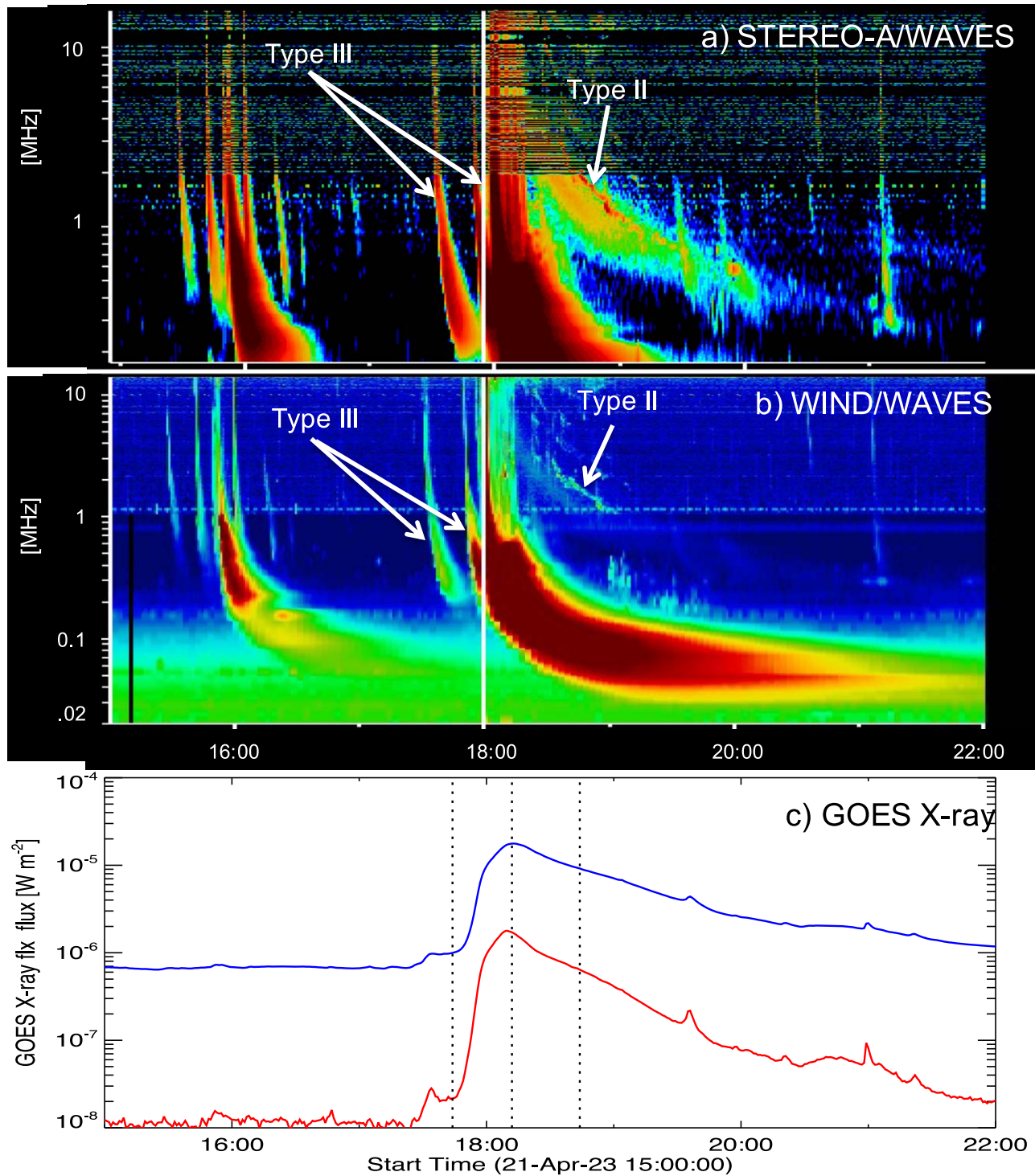

Figure 2. Emission signatures of the CME eruption from AR 13283. (a) Radio dynamic spectrum obtained from WAVES on board STA. Arrows point to the type II and III radio burst triggered by the eruption. (b) Radio dynamic spectrum obtained by WIND/WAVES instrument located at the Lagrange L1 point. The arrows refer to the type III bursts originating from the CME-associated flare. (c) Disk-integrated GOES X-ray flux. The peak value of the flux refers to the M1.7 class flare from AR 13283. The vertical dotted lines refer to the flare start (17:44 UT), peak (18:12 UT), and end (18:44 UT) times.

The time evolution of the net magnetic flux is plotted in Figure 5(a). The net flux in the north (south) polarity is around 6×10^{21} Mx (8×10^{21} Mx). These fluxes are half of the values typically noted in growing ARs that consist of large-scale sunspot polarities (Vemareddy & Démoulin 2017; Vemareddy 2019). The net flux profile increases during the first half of April 20, corresponding to the flux emergence, and 12 hr before the eruption, the net flux decreases by 1×10^{21} Mx in each polarity.

From the velocity and magnetic fields, we also calculated the helicity injection rate (dH/dt) to evaluate the net helicity coming from the flux motions (Démoulin & Berger 2003; Vemareddy et al. 2012a; Vemareddy & Démoulin 2017). The dH/dt and H with time are plotted in Figure 5(b). The dH/dt profile evolves with positive values around a mean value of 3.5×10^{36} Mx^2 s^{-1} until April 21, after which it becomes marginally negative, and it then oscillates around zero values. The flux emergence phase is
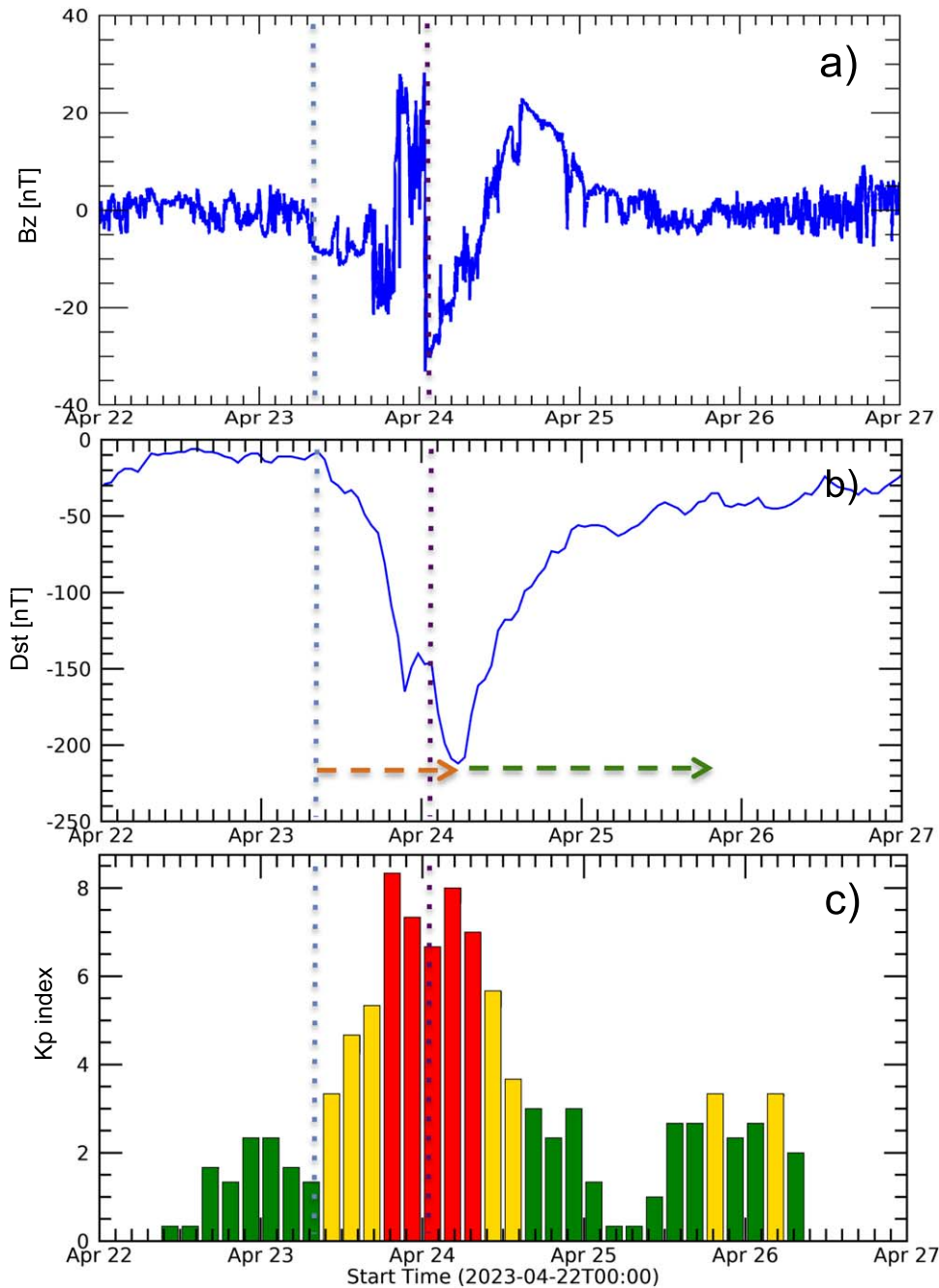
Figure 3. In situ observations of the CME as it encountered the Earth's atmosphere. (a) Bz-component of the magnetic field with time. The Bz started to become negative at around 07:30 UT on April 23. The dotted vertical blue and magenta lines correspond to the shock (23/07:30 UT) and MC (24/01:00 UT) arrival times. (b) Dst index with time. The Dst index started to decrease to negative values around 08:30 UT on April 23. It peaked at -212 nT at 05:30 UT on 2023 April 24, indicating an intense and long-duration geomagnetic storm. The main phase of the storm (dashed orange arrow) persisted for 22 hr, followed by a long recovery phase of several days. (c) Histogram of the Kp index values. The red, yellow, and blue bars refer to index values 0–3, 3–6, and 6–9, respectively. The Kp index values reach up to eight during the main phase of the storm, indicating an intense geomagnetic storm of G4 severity according to the space-weather classification.

seen to pump additional helicity flux above the mean value. A positive sign of helicity refers to the right-hand helicity of the magnetic structure, which also agrees with the windings of the filament threads (Figure 6). During the four days of evolution, the flux motions accumulate a coronal helicity of 0.9×10^{42} Mx^2. It is worth pointing out that the filament channel was present well before April 18, and therefore, a magnetic structure exists with preaccumulated helicity in the corona. Accounting for the net average flux in the AR as 7×10^{21} Mx, the average twist of the flux tube (H/Φ^2) could be 0.02–0.1 turns, which is in the range of

several erupting ARs (Vemareddy 2019). In conclusion, the large shear and converging motions build the twisted flux about the PIL, which was set to erupt during the phase when flux motions started to inject weak helicity flux with an alternate polarity into the AR corona.

3.2. Initiation and Onset of the CME Eruption

The magnetic evolution in the AR is favorable for the eruption of twisted fields. Before the four days of the eruption,
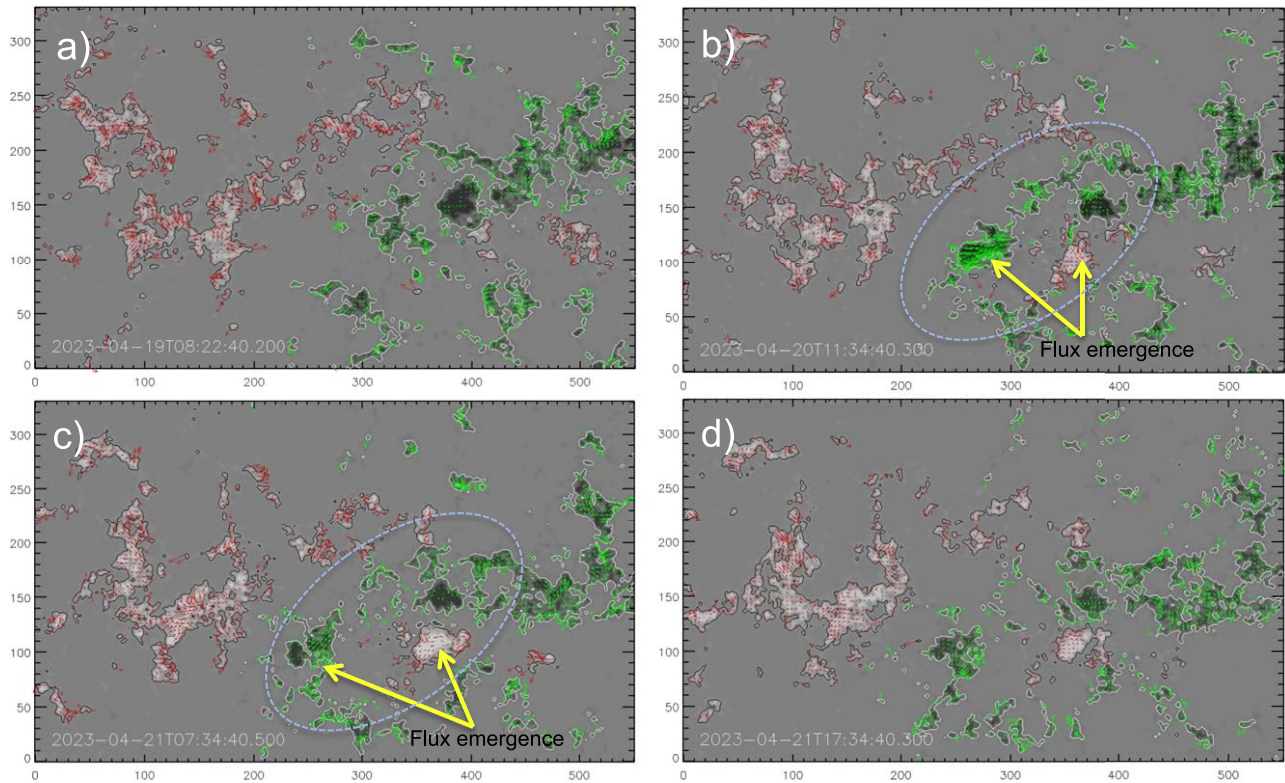
Figure 4. Horizontal velocity of the flux motions in AR 13283. The background image is the B_z map with contours ±150 G. The arrows indicate the direction of motion, and their length is proportional to a magnitude of 0.7 km s^{-1} at most. Large shear motions of the fluxes can be noted in the region enclosed by blue ovals. Fluxes also emerge and move apart during the evolution. In all panels, the axis units are in pixels of 0.″5.

a long filament channel already existed, lying above the PIL. One of its leg lies in the leading negative polarity, and the other leg lies at the extreme east edge of the following positive polarity. Figure 6 displays the EUV images showing the filament and the surrounding loops. These images reveal the orientation of the filament axis and the PIL, which are found in a southeast to northwest direction at a tilt angle of 30°. The filament threads, which are wound in the right-hand direction, are clearly visible along the filament channel. The winding direction reflects the right-handed helicalness or positive helicity of the magnetic field, in agreement with the sign of the helicity injection estimates. The overall shape of the filament is a forward S-shape, which indicates positive helicity and is compatible with the hemispheric rule of sigmoids being in the south hemisphere.

About two hours before the main eruption, the filament channel shows signs of eruption, such as a brightening along its length, threads that were reorganized, and the surrounding loop structures, which were heightened. The initiation of the eruption started at around 17:42 UT, with the subfilament section along the PIL starting to rise. This means that the large-scale filament is a combination of subtwisted loop systems originating from different locations along the PIL. With this rise, the GOES X-ray flux also increases, commencing the flare at 17:44 UT. Figure 5 delineates the rising filament section and the two flare ribbons at 17:56 UT. In order to visualize the filament and the surrounding loop system, we analyze running-difference images, as displayed in Figure 7. The AIA 304 Å difference images clearly show the rising filament section with time and its disappearance after 18:03 UT, whereas the AIA 171 and 193 difference images give the impression of a blob-like structure that expands, which forms

an oval shape in exactly the same direction as the PIL, i.e., southeast to northwest. Further rise motion brought the filament into the phase of the onset of its eruption, and this was clearly associated with the formation of the cusp-shaped loops underneath the expanding filament. The start of the filament rise motion at 17:42 UT and its onset at 18:03 UT fall into the scenario of tether-cutting reconnection (Moore et al. 2001). The reconnection of the surrounding less strongly sheared loops adds more field to the filament, which is regarded as the MFR, and the main phase of the eruption occurs as a result of the runaway tether-cutting reconnection, which is linked to strong flare ribbons at the peak flare time. This eruption scenario is illustrated in the right panels of Figure 7, with the orange curve representing the erupting filament and the overlying loops undergoing reconnection as pink curves. With the benefit of vantage point observations, these eruptions are being investigated more thoroughly, in particular, the kinematics of slow and fast rising motion (Vemareddy et al. 2012b, 2022).

3.3. Near-Sun Rotation of the MFR

To determine the underlying large-scale structure and orientation of the MFR, we exploited the plane-of-sky-projected coronagraph images from different vantage points. For this purpose, we employed the graduated cylindrical shell (GCS; Thernisien et al. 2009) model. In this model, the large-scale structure of the MFR is approximated either by the conical legs or by the curved (tubular) fronts. The model is based on height-aspect ratio (κ), half-angle (α), tilt angle (γ), latitude (θ), and longitude (ϕ). The underlying assumption of this model is that the preeruptive magnetic configuration of the source AR constrains the magnetic orientation of an erupting
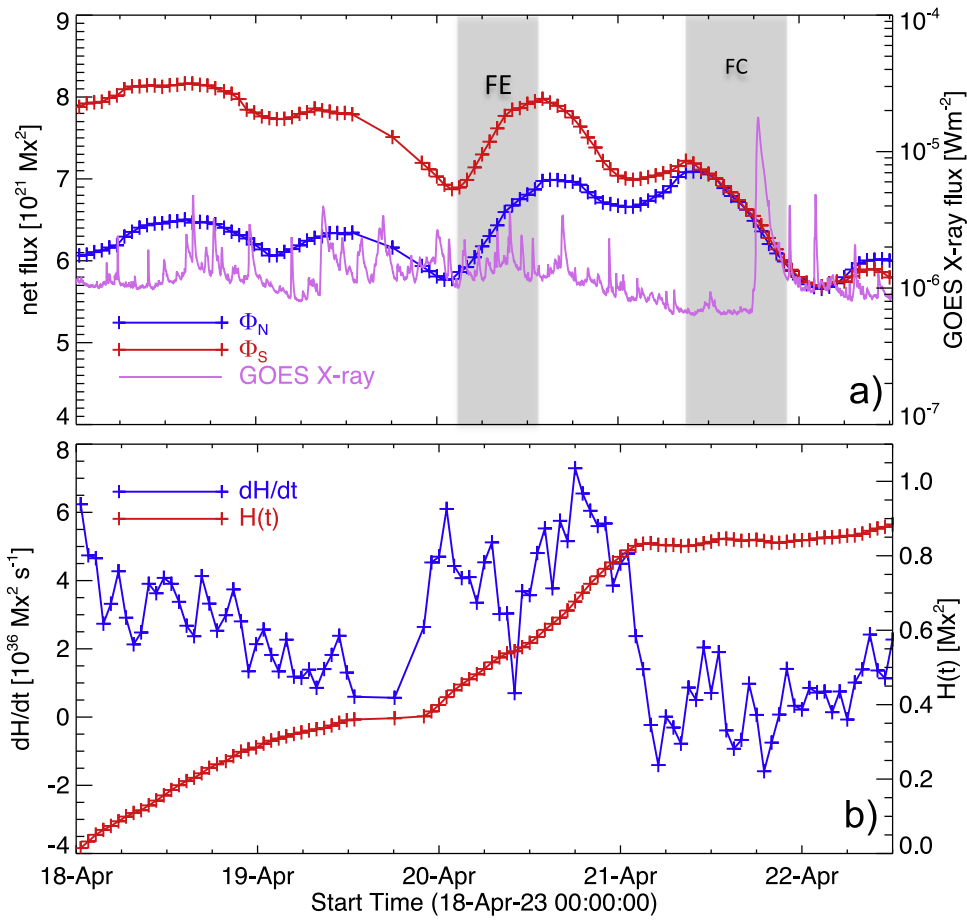
Figure 5. Magnetic evolution in AR 13283. (a) Net flux in positive (north) and negative (south) magnetic polarities. The disk-integrated GOES X-ray (1.0–8.0 Å passband) flux is also shown with the y-axis scale on the right. The gray bands refer to the phase of the flux emergence (FE) and flux cancellations (FC) by converging motions. Note that the M1.7 flare is associated with the fast CME that occurred during the converging and canceling of the flux motions. (b) Helicity injection rate (dH/dt) with time. The accumulated helicity, $H(t)$, is also plotted with a y-axis scale on the right side.
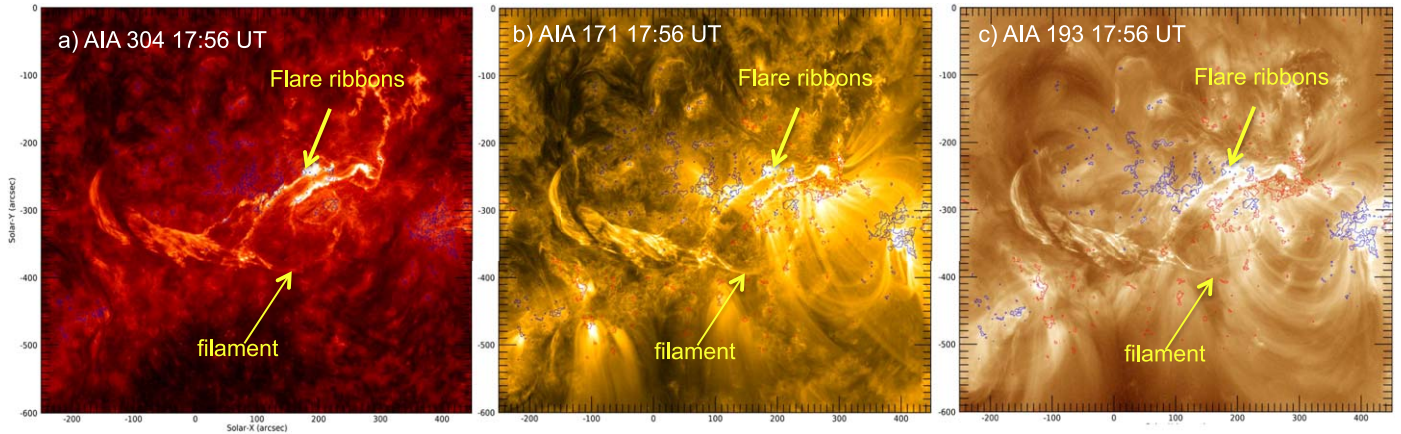
Figure 6. EUV images during the onset of the eruption. (a) AIA 304 Å Image showing the filament section as it rises. Flare ribbons are formed on each side of the PIL. (b)–(c) AIA 171 and 193 Å images show the erupting filament. In all panels, contours of Bz (±150 G) are overlaid. These images reveal the filament threads, which are wound in the right-hand direction.

MFR. This is based on an analysis of several CMEs and the magnetic configurations of their source regions (Cremades & Bothmer 2004), which is incorrect in a number of observed cases.

In Figure 8 we display the difference images of STA/COR2, LASCO/C2, and C3, obtained at two different epochs. The wire frame (dotted green) from the GCS fit is overlaid on these

panels. Since the SoHO and STA spacecraft are separated by 10°, the morphology of the CME is observed to be similar from the two different vantage points. The GCS fit to the CME morphology is implemented with the GUI procedure `rtsccguicloud.pro`, which is available in the STEREO tree of the SSWIDL software (Freeland & Handy 1998). While fitting the GCS model, the tilt angle of the erupting feature and
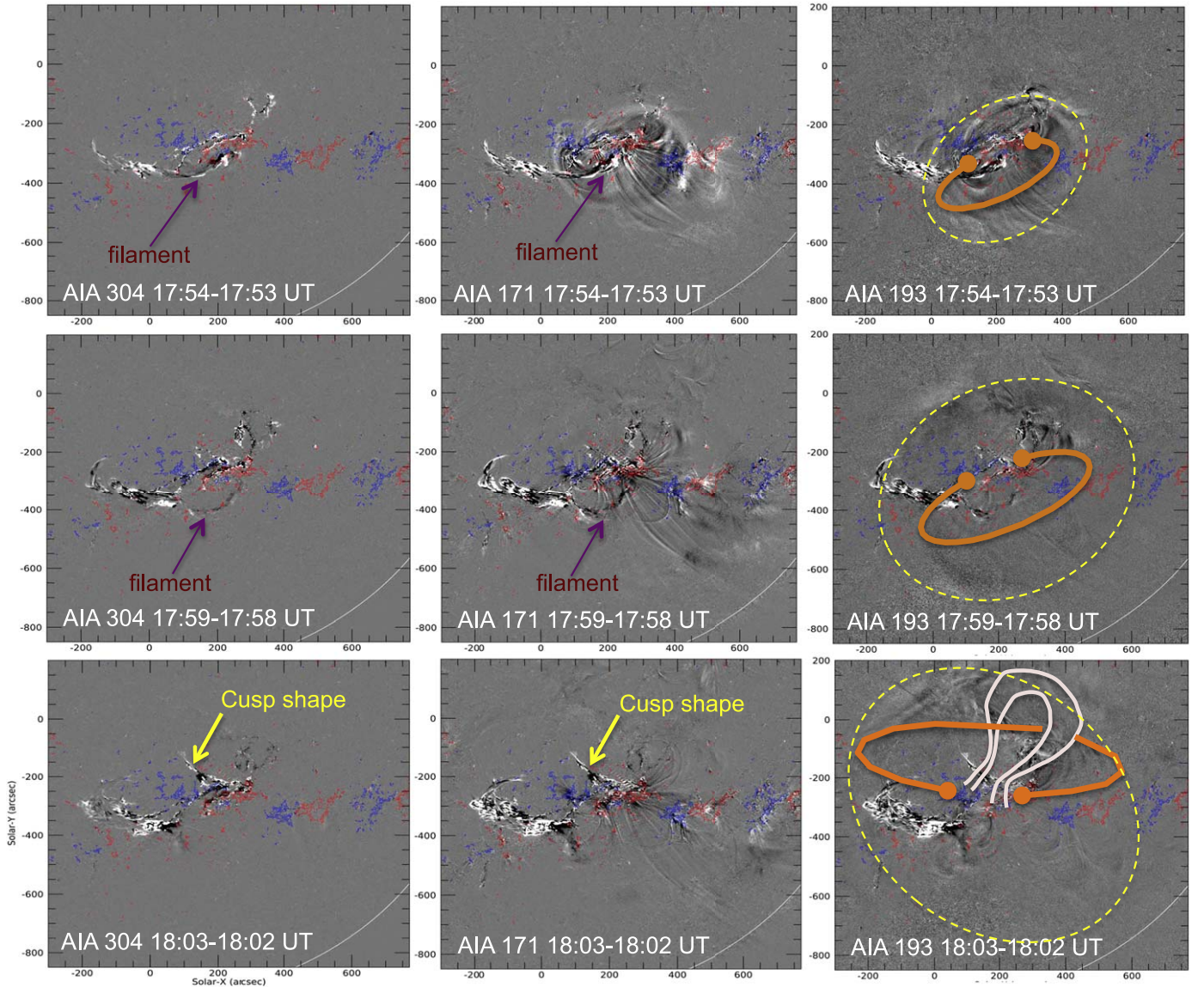
Figure 7. Onset of the eruption from AR 13283. Left column: AIA 304 Å difference images showing the rising filament section at different times. A cusp is formed underneath the rising filament after 18:02 UT. Middle column: AIA 171 Å difference images showing the rising filament and the oval shape disturbance due to the rising filament as a blob-like structure. Right column: AIA 193 Å difference images showing the oval disturbance surrounding the environment of the rising filament. The eruption scenario is illustrated in the panels, with the orange curve representing the erupting filament and the overlying loops undergoing reconnection as pink curves. All panels are overlaid with Bz contours at ±150 G. To better understand the eruption onset, the image sequence from 17:51 to 18:04 UT is attached as a video.

(An animation of this figure is available.)

the PIL orientation in the source region are generally considered because the erupting feature (filament or prominence) is assumed to be the MFR. However, we note that the PIL orientation (southeast to northwest) in the source region is quite different from the CME morphology, which is in a northeast to southwest direction. It appears that the MFR (erupting feature) from the source region has rotated by about $60°$. Therefore, we use this information to set the tilt angle by visually matching the observed CME morphology. From this fit, the tilt angle is found to vary from $-20°$ to $-25°$ while the CME evolves from 18:36 UT to 20:36 UT. Moreover, the corresponding heights are noted as $10\,R_\odot$ and $27\,R_\odot$, respectively. From these two heights in time, we found that the CME velocity in 3D space exceeds $1500\,\mathrm{km\,s^{-1}}$.

3.4. Propagation of the CME

After the first emergence of the CME in the LASCO C2 FOV at 18:12 UT, its propagation in the C3 and COR2 is very clearly observed in the running-difference images. Because of the line-of-sight propagation, the CME motion in these images only represents lateral expansion. The further propagation of the CME is tracked in the wide-angle observations of HI1 and HI2 of STA. The running-difference images of individual instruments are combined to make a composite running-difference image at each instant in time so that the heliospheric propagation of the CME is visualized continuously while it transits from one FOV to the next up to $370\,R_\odot$. In Figure 9 we display these composite running images at four epochs. The bright shock front is evident, along with the CME leading edge
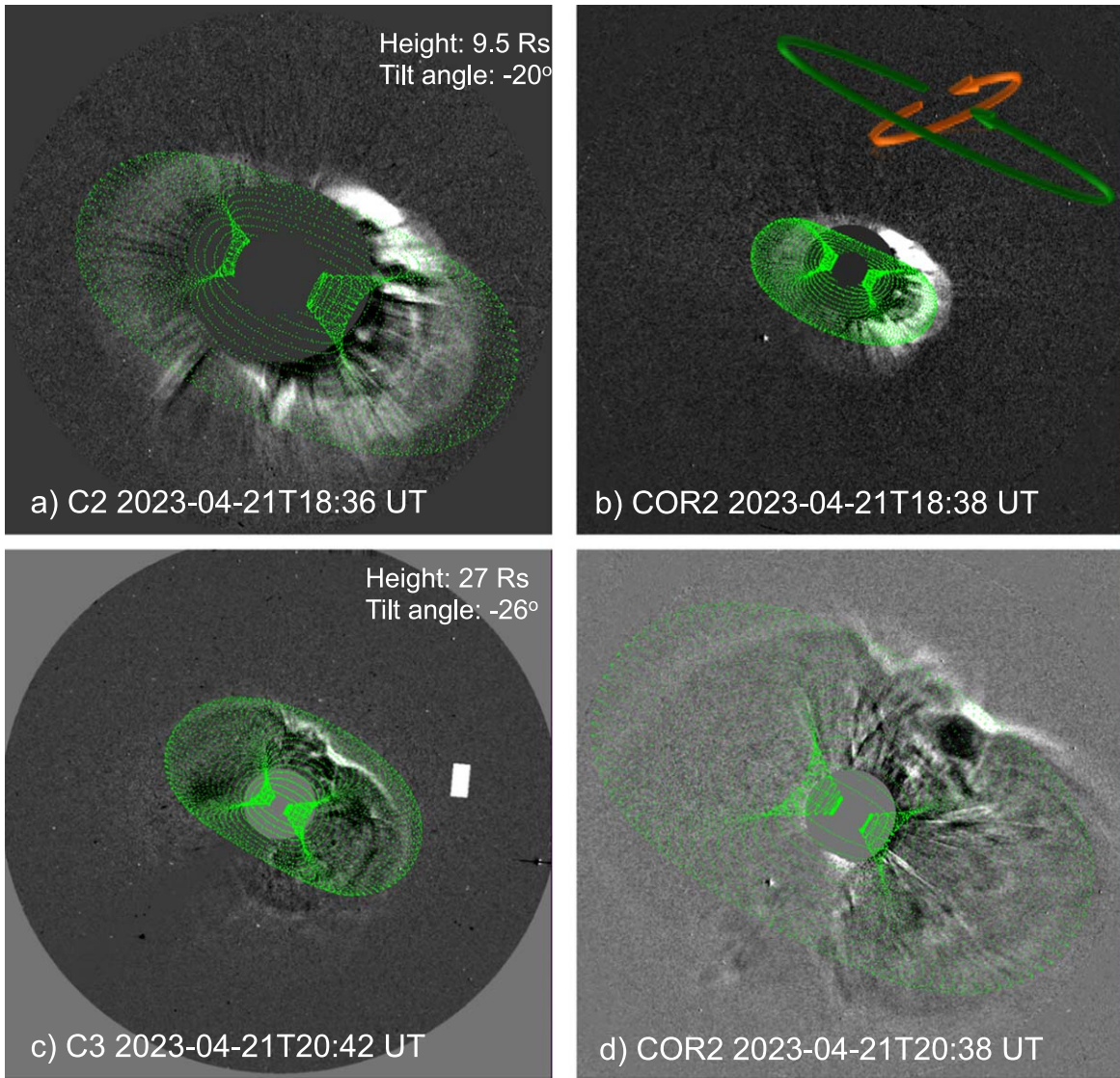
Figure 8. GCS fit to CME morphology observed from COR2 and LASCO. (a)–(b) CME morphology observed from C2 and COR2 at 18:36 UT and 18:38 UT respectively. The MFR axis orientation is indicated as seen in the source region (orange) and from LASCO (green). (c)–(d) CME morphology observed from C3 and COR2 at 20:36 UT and 20:38 UT, respectively. In all the panels, the best-fit wire frame of the MFR in the GCS model is overplotted. Since the STA and SoHO are separated at 10°, the CME morphology is similar in both views. Importantly, the MFR oriented from northeast to southwest direction with a tilt angle of $-20°$ at 18:36 UT and $-26°$ at 20:36 UT. Compared to the source region PIL, the filament apex appears to be rotated by about 56° during its eruption as a CME within $10\,R_\odot$.

in HI2. However, it is difficult to identify the precise boundaries of the CME core and leading edge. The morphology is not spherically symmetric, but a cone shape that is inclined roughly about 25° to the ecliptic plane, consistent with the near-Sun CME orientation.

The event is also cataloged in the HELCATS list,[2] providing useful kinematic information from the analysis of the time-elongation map (J-map) constructed from combined difference images (Sheeley et al. 1999; Davies et al. 2009), as displayed in Figure 10(a). The time elongation in terms of height is plotted in Figure 10(b). We also plot the height–time data obtained from the LASCO CME catalog[3]. A second-order polynomial function fits these observed height–time data of the CME propagation best. Starting from a velocity of $1459\,\mathrm{km\,s^{-1}}$, the

CME decelerates at a rate of $14\,\mathrm{m\,s^{-2}}$ in the LASCO FOV. At the height of $20\,R_\odot$, the velocity of the CME is $1226\,\mathrm{km\,s^{-1}}$. In the HI FOV, the travel time for a distance of 1 au corresponds to 33 hr (3:00 UT on April 23) from the CME onset at 18:00 UT on April 21. The difference of 4.5 hr compared to the observed arrival time of the ICME shock is due to projection effects. This emphasizes the difficulty of tracking the earthward propagation of the CME in this case.

Since the CME launched at 20:30 UT on April 21 at the Sun, the arrival time of the shock front is 35 hr. As a geomagnetic storm commences at the same time as the arrival of the shock front, it is important to assess the arrival time of the frontal structure of the CME, which is the ICME shock front. We use the initial CME speed at $20\,R_\odot$ in the drag-based model. A drag coefficient $\gamma = 0.15 \times 10^{-7}\,\mathrm{km^{-1}}$ and a background solar wind speed of $400\,\mathrm{km\,s^{-1}}$ are also used. For the observed $1226\,\mathrm{km\,s^{-1}}$ speed, the transit time exactly matches the arrival of the ICME sheath. Any higher value of the drag coefficient
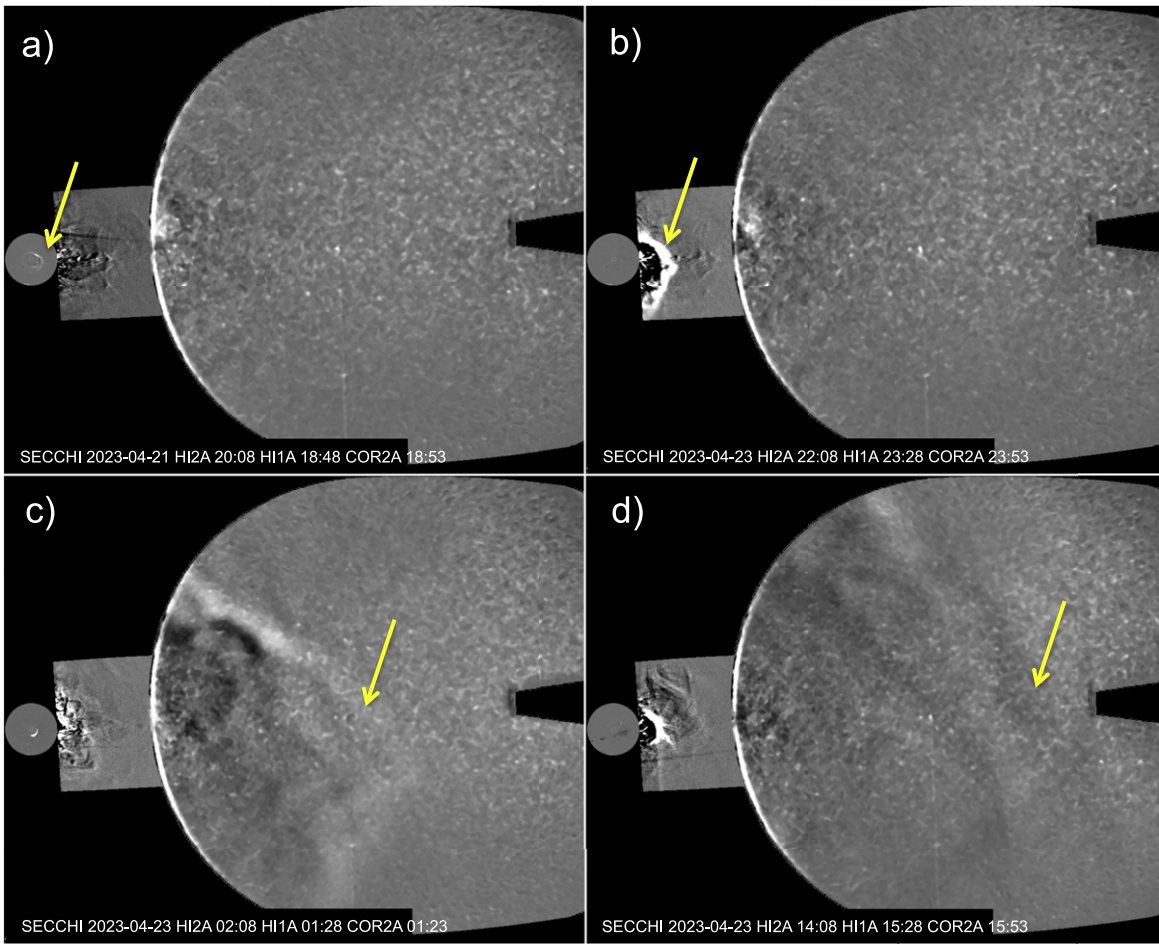
Figure 9. CME propagation from the low corona into the heliosphere. (a)–(d) Combined running-difference images of STA/COR2 (2.5–15 $R_\odot$), STA/HI1 and STA/HI2 during 2023 April 21–23. The yellow arrow points to the leading edge of the CME at different epochs of its propagation. Because the CME propagated toward the STA spacecraft, the propagation in the images mostly represents the lateral expansion of the CME. The sequence of images displayed in each panel is attached as a video stream.

(An animation of this figure is available.)

may require a higher value of the CME speed to match its observed in situ arrival.

3.5. In Situ Magnetic Field Observations

The WIND observations of the in situ magnetic field are plotted in Figure 11. These observations are one-minute averaged in the geocentric solar ecliptic coordinate system. The shock front encountered the spacecraft at 07:30 UT on April 23. Following the ICME shock-sheath region, the MC passes, which is identified by the systematic variation of the magnetic field components, indicating a strong magnetic field (30 nT) associated with an MFR-like structure. The Bz-component rotates, with its sign changing from negative to positive. Furthermore, the solar wind velocity increases from background values of around $360\,\mathrm{km\,s^{-1}}$. Based on these observations, we identified the time intervals for the MC as 01:00–15:00 UT on April 24.

The MC signatures are often modeled by an MFR. We employ the Lundquist (1950) and Gold & Hoyle (GH; 1960) models of cylindrically symmetric linear force-free magnetic fields. Because the MC grows during transit, the fitting technique takes this into consideration (Vemareddy et al. 2016). The magnetic field profile along the observational path of the spacecraft in the Lundquist model is determined by the

orientation of the flux rope axis, i.e., the elevation and azimuth angle (θ and ϕ), the closest approach of the observational path p, the flux rope diameter D, the helicity sign H, and the field strength B_0 at the flux rope center (Lepping et al. 1990). In the GH model, the twist parameter T_0 is added to these parameters. The helicity sign is decided on a trial basis; in this case, it is positive and consistent with the helicity sign of the source region, and the rest of the parameters are determined when the fitting converges in the least-squares sense. As a measure of the goodness of fit, we compute the root-mean-square (rms) deviation (rms $= \sqrt{\sum_{i=1,N}(\boldsymbol{B}_o(t_i) - \boldsymbol{B}_m(t_i))^2/N}$) between the observed magnetic field ($\boldsymbol{B}_o(t_i)$) and the modeled field ($\boldsymbol{B}_m(t_i)$) (Marubashi & Lepping 2007). In terms of the rms value, the GH fit (rms $= 6.76$) is a better model than the Lundquist model (rms $= 9.49$) as compared to the observations in Figure 11. Based on these fits, the MC axis is oriented $-15°$ in latitude and roughly $260°$ in longitude. These results indicate that the MC magnetic fields had a significant southward Bz-component to launch the geomagnetic storm. The flux rope has a positive magnetic helicity, which is in line with the source region helicity sign of the erupting part of the filament as seen in EUV images (Figure 6). The twist of the magnetic field in the GH flux rope model is 1.67 turns au^{-1}. The MC has a diameter of 0.17 au. While passing the spacecraft, the radius of the MC
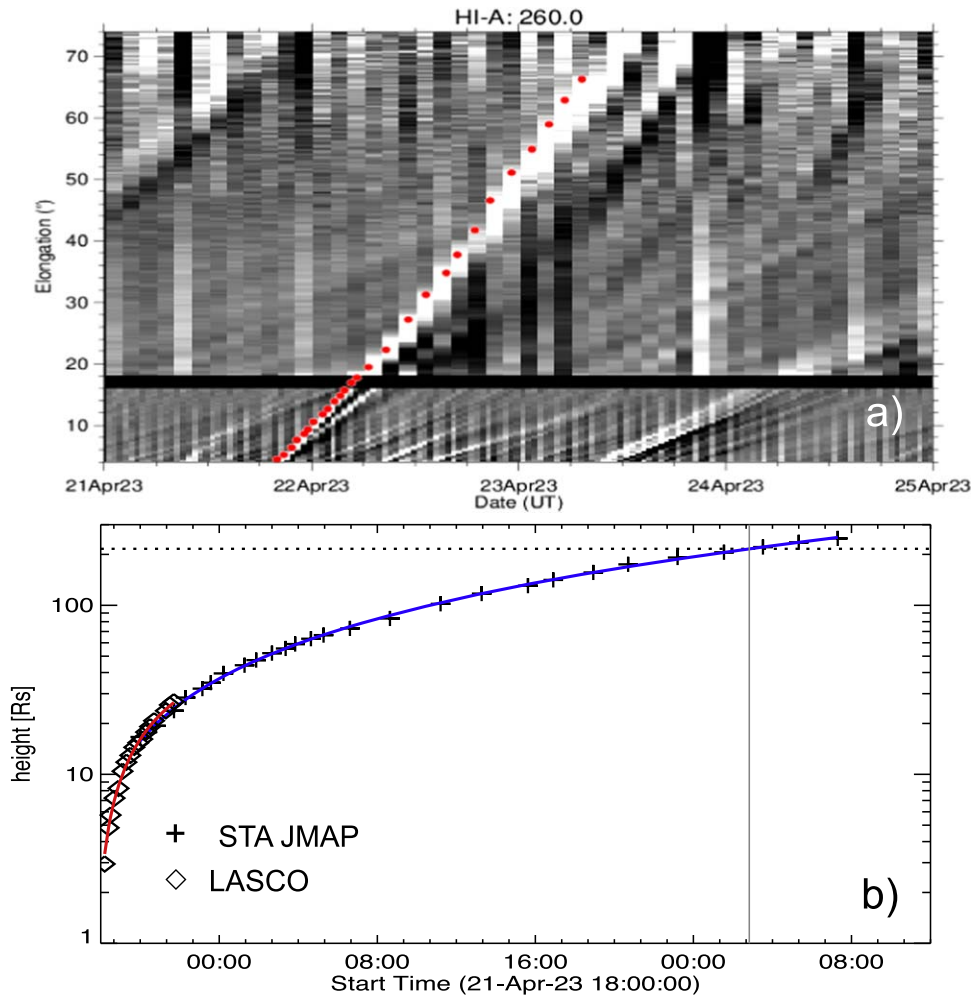
Figure 10. CME kinematics in the plane-of-sky observations. (a) Time-elongation map (J-map) constructed from the slices at a position angle of 260°. The red dots are the trace of the leading edge of the propagating CME. (b) Height–time of the CME. The red curve is a second-order fit to the LASCO data (diamond), and the blue curve is a second-order fit to the J-map data (plus). The Sun–Earth distance is shown with the horizontal dotted line, and the vertical gray line represents the time (23/02:50 UT) of the Sun–Earth distance passage in the plane of sky.

varied with time: $r(t) = r_0(1 + Et)$, where E is the expansion rate, which is determined to be 0.09 per day from the MC fitting analysis.

4. Summary and Discussion

We investigated the CME eruption that occurred on 2023 April 21, which caused a severe geomagnetic storm on 2023 April 23. The eruption originated from solar AR 13283 near the disk center. The AR was in its decay stage, with fragmented polarities and a preexisting long filament channel a few days before the eruption. The polarities underwent large-scale shear and converging motions, so that the flux cancellation led to the buildup of twisted flux threads along the main PIL. The magnetic helicity is positive, so that the chirality of the filament threads is right-handed. Importantly, the helicity injection changed from a positive to a negative sign early on April 21. Because the flux rope (filament) was built up by monotonous helicity accumulation over several days (Amari et al. 2003; Vemareddy & Mishra 2015), the further converging and canceling fluxes led to a change in the helicity injection and to the unstable nature of the MFR and its further eruption.

The filament that is initiated to erupt is part of the long, multiply threaded filament channel. Along with the increase in

GOES X-ray flux, the filament set to rise at 17:42 UT that eventually erupted at around 18:03 UT (see Table 1). Importantly, the CME morphology revealed that the MFR is oriented in the northeast to southwest direction (−26° with respect to the equator), which differs by 56° from the filament orientation, which is in the southeast to northwest direction (30° with respect to the equator). These observations imply that the filament apex rotates in a clockwise direction owing to the right-hand twist of the magnetic field (Lynch et al. 2009; Green et al. 2011).

The CME decelerates in the LASCO FOV and has a velocity of 1226 km s^{-1} at 20 $R_\odot$. In the H I FOV, the CME lateral expansion is tracked more than the earthward motion, and therefore, the arrival time estimation is difficult to assess. However, the drag-based model gives correct estimates of the arrival time of the ICME sheath with the initial CME speed at 20 $R_\odot$. The in situ arrival of the ICME shock was at 07:30 UT on April 23, and then a geomagnetic storm commenced at 08:30 UT. The flux rope fitting to the in situ magnetic field observations revealed that the MC flux rope orientation is consistent with its near-Sun orientation within 10 $R_\odot$, which has a significant negative Bz-component. The analysis of this study indicates that the near-Sun rotation of the filament during its
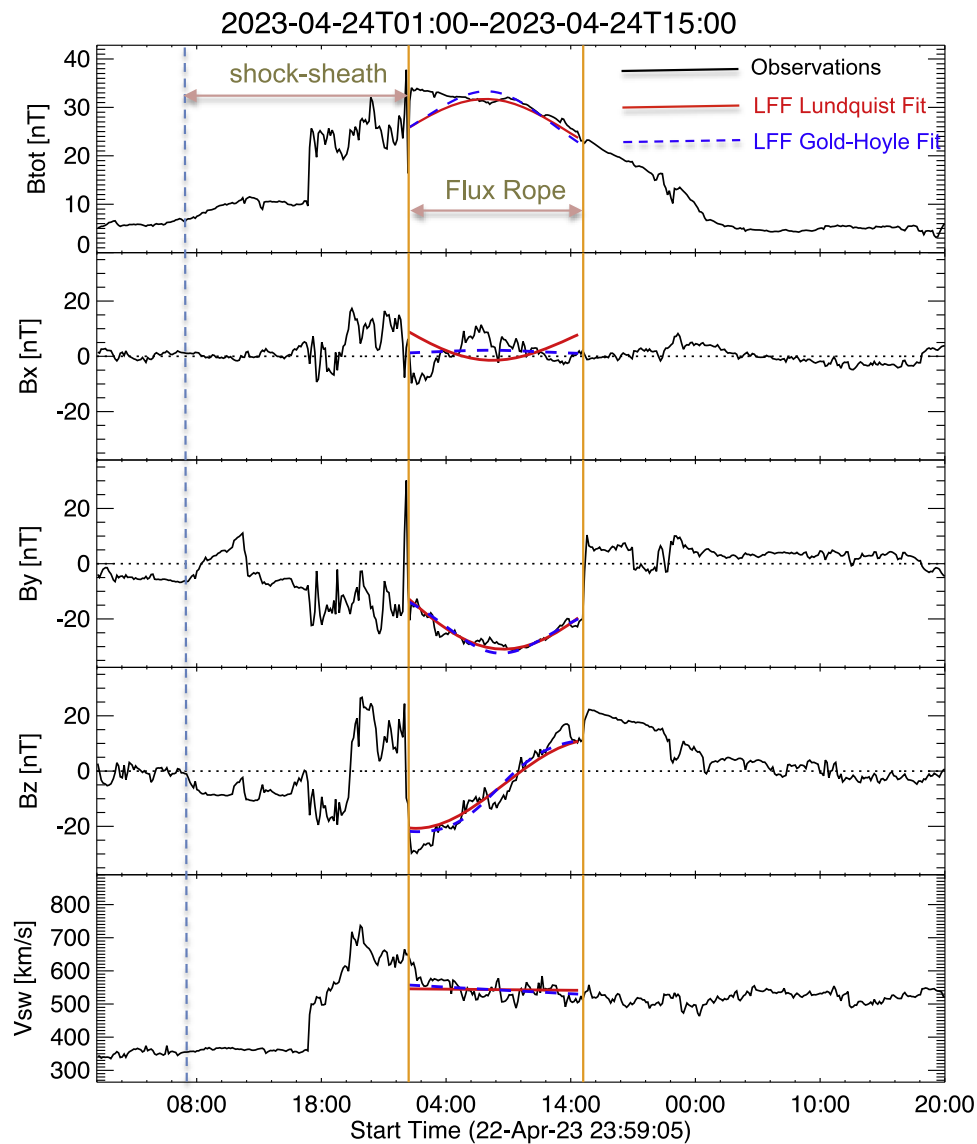
Figure 11. In situ observations of the CME (ICME) from the WIND spacecraft. The panels from top to bottom show plots of the magnetic field strength (B_{tot}) and its components (B_x, B_y, and B_z), and the solar wind speed (V_{sw}) as a function of time. The dashed vertical blue line marks the arrival time of the shock (23/07:30 UT) at the spacecraft, and the vertical orange lines correspond to the MC start and end times. The blue and red curves are the fitting results of the Gold–Hoyle and Lundquist models, respectively. The fitting yields MC orientations of $-5°$ and $-15°$ latitude, respectively, indicating a mostly southward B_z-component.

Table 1
Chronology of the CME Eruption from AR 13283

21/17:44 UT	CME initiation and flare start time
21/18:03 UT	Onset of CME eruption
21/18:12 UT	peak time of M1.7 flare
21/20:30 UT	CME LE at a height 20 $R_\odot$
23/07:30 UT	ICME shock arrival
24/01:00–15:00 UT	MC passage
23/08:30 UT	geomagnetic storm commencement
24/05:30 UT	geomagnetic storm peaked at 212 nT

eruption to the CME is the key to the negative B_z-component, and consequently, to the intense geomagnetic storm.

ORCID iDs

P. Vemareddy ⓘ https://orcid.org/0000-0003-4433-8823

References

Amari, T., Luciani, J. F., Aly, J. J., et al. 2003, ApJ, 595, 1231
Bougeret, J. L., Kaiser, M. L., Kellogg, P. J., et al. 1995, SSRv, 71, 231
Brueckner, G. E., Howard, R. A., Koomen, M. J., et al. 1995, SoPh, 162, 357
Cane, H. V., Sheeley, N. R. J., & Howard, R. A. 1987, JGR, 92, 9869

Canfield, R. C., Hudson, H. S., & McKenzie, D. E. 1999, GeoRL, 26, 627
Cargill, P. J. 2004, SoPh, 221, 135
Cheng, X., Zhang, J., Ding, M. D., et al. 2013, ApJL, 769, L25
Cremades, H., & Bothmer, V. 2004, A&A, 422, 307
Davies, J. A., Harrison, R. A., Rouillard, A. P., et al. 2009, GeoRL, 36, 2102
Démoulin, P., & Berger, M. A. 2003, SoPh, 215, 203
Freeland, S. L., & Handy, B. N. 1998, SoPh, 182, 497
Gold, T., & Hoyle, F. 1960, MNRAS, 120, 89
Gopalswamy, N., Lara, A., Yashiro, S., et al. 2001, JGR, 106, 29207
Gopalswamy, N., Mäkelä, P., Xie, H., Akiyama, S., & Yashiro, S. 2009, JGRA, 114, A00A22
Gopalswamy, N., Mäkelä, P., & Yashiro, S. 2019, SunGe, 14, 111
Gopalswamy, N., Shimojo, M., Lu, W., et al. 2003, ApJ, 586, 562
Gopalswamy, N., Yashiro, S., & Akiyama, S. 2007, JGRA, 112, A06112
Gopalswamy, N., Yashiro, S., Akiyama, S., et al. 2022, JGRA, 127, e30404
Gosling, J. T. 1993, JGR, 98, 18937
Gosling, J. T., McComas, D. J., Phillips, J. L., & Bame, S. J. 1991, JGR, 96, 7831
Green, L. M., Kliem, B., & Wallace, A. J. 2011, A&A, 526, A2
House, L. L., Wagner, W. J., Hildner, E., Sawyer, C., & Schmidt, H. U. 1981, ApJL, 244, L117
Howard, R. A., Moses, J. D., Vourlidas, A., et al. 2008, SSRv, 136, 67
Illing, R. M. E., & Hundhausen, A. J. 1985, JGR, 90, 275
Isavnin, A., Vourlidas, A., & Kilpua, E. K. J. 2013, SoPh, 284, 203
Kaiser, M. L., Kucera, T. A., Davila, J. M., et al. 2008, SSRv, 136, 5
Kay, C., Gopalswamy, N., Xie, H., & Yashiro, S. 2017, SoPh, 292, 78
Lemen, J. R., Title, A. M., Akin, D. J., et al. 2012, SoPh, 275, 17
Lepping, R. P., Burlaga, L. F., & Jones, J. A. 1990, JGR, 95, 11957
Lundquist, S. 1950, Ark. Fys., 2, 361
Lynch, B. J., Antiochos, S. K., Li, Y., Luhmann, J. G., & DeVore, C. R. 2009, ApJ, 697, 1918
MacQueen, R. M., Eddy, J. A., Gosling, J. T., et al. 1974, ApJL, 187, L85

Marubashi, K., & Lepping, R. P. 2007, AnGeo, 25, 2453
Moore, R. L., Sterling, A. C., Hudson, H. S., & Lemen, J. R. 2001, ApJ, 552, 833
Schuck, P. W. 2005, ApJL, 632, L53
Sheeley, N. R., Walters, J. H., Wang, Y. M., & Howard, R. A. 1999, JGR, 104, 24739
Sheeley, N. R. J., Michels, D. J., Howard, R. A., & Koomen, M. J. 1980, ApJL, 237, L99
Srivastava, N., & Venkatakrishnan, P. 2004, JGRA, 109, A10103
Thernisien, A., Vourlidas, A., & Howard, R. A. 2009, SoPh, 256, 111
Török, T., & Kliem, B. 2003, A&A, 406, 1043
Vasantharaju, N., Vemareddy, P., Ravindra, B., & Doddamani, V. H. 2019, ApJ, 874, 182
Vemareddy, P. 2019, ApJ, 872, 182
Vemareddy, P., Ambastha, A., Maurya, R. A., & Chae, J. 2012a, ApJ, 761, 86
Vemareddy, P., & Démoulin, P. 2017, A&A, 597, A104
Vemareddy, P., Démoulin, P., Sasikumar Raja, K., et al. 2022, ApJ, 927, 108
Vemareddy, P., Gopalswamy, N., & Ravindra, B. 2017, ApJ, 850, 38
Vemareddy, P., Maurya, R. A., & Ambastha, A. 2012b, SoPh, 277, 337
Vemareddy, P., & Mishra, W. 2015, ApJ, 814, 59
Vemareddy, P., Möstl, C., Amerstorfer, T., et al. 2016, ApJ, 828, 12
Vemareddy, P., & Zhang, J. 2014, ApJ, 797, 80
Vourlidas, A., Lynch, B. J., Howard, R. A., & Li, Y. 2013, SoPh, 284, 179
Vršnak, B., Žic, T., Falkenberg, T. V., et al. 2010, A&A, 512, A43
Webb, D. F., Cliver, E. W., Crooker, N. U., Cry, O. C. S., & Thompson, B. J. 2000, JGR, 105, 7491
Webb, D. F., & Howard, T. A. 2012, LRSP, 9, 3
Webb, D. F., & Hundhausen, A. J. 1987, SoPh, 108, 383
Zhang, J., Cheng, X., & Ding, M.-D. 2012, NatCo, 3, 747
Zhang, J., Dere, K. P., Howard, R. A., & Vourlidas, A. 2004, ApJ, 604, 420
Zhang, J., Richardson, I. G., Webb, D. F., et al. 2007, JGRA, 112, A10102
Zhang, J., Temmer, M., Gopalswamy, N., et al. 2021, PEPS, 8, 56